Supporting Information

Ultrafast electron transfer in 2D/2D g-C_3N_4/WO_3 S-scheme heterojunctions for enhanced H_2O_2 production

Ping Li [a], Liang Wei [a], Wei Xia [b], Chengcheng Yuan [c], Chenbin Ai [c], Meng Li [a,*]

[a] *Guangxi Key Laboratory of Natural Polymer Chemistry and Physics, Nanning Normal University, Nanning 530001, Guangxi, China*

[b] *School of Resources and Environment Engineering, Moutai Institute, Renhuai 564507, Guizhou, China*

[c] *Laboratory of Solar Fuel, Faculty of Materials Science and Chemistry, China University of Geosciences, Wuhan 430078, Hubei, China*

** Corresponding author. E-mail: limeng_2016@126.com (M. Li).*

1. Characterization

The crystalline phase of the synthesized samples was characterized by X-ray diffraction (XRD; Shimadzu XRD-6100, Japan) using Cu K_α radiation. Morphological analysis was conducted using field emission scanning electron microscopy (FESEM; Hitachi Regulus 8100, Japan). Further microstructural details were obtained by transmission electron microscopy (TEM) and high-resolution TEM (HRTEM) on a JEOL JEM-2100F instrument (Japan). Specific surface area was determined by the Brunauer–Emmett–Teller (BET) method from N_2 adsorption–desorption isotherms measured on a Micromeritics ASAP 2020 analyser (USA). UV–visible diffuse reflectance spectra were acquired using a Shimadzu UV-2550 spectrophotometer (Japan). Steady-state photoluminescence (PL) spectra were recorded on a Hitachi F-7000 fluorescence spectrophotometer, while time-resolved photoluminescence (TRPL) decays were measured using an Edinburgh Instruments FLS 1000 spectrometer (UK). Chemical states were probed by in situ and ex situ X-ray photoelectron spectroscopy (XPS) using a Thermo Scientific Escalab 210 instrument with Al K_α radiation. Electron paramagnetic resonance (EPR; Bruker MEX-nano) with 5,5-dimethyl-1-pyrroline-N-oxide (DMPO) as the spin trap was employed to detect reactive oxygen species (· OH and · O_2^-) generated during photocatalytic processes. Fourier transform infrared (FTIR) spectra and in situ diffuse reflectance infrared Fourier transform spectroscopy (DRIFTS) were collected on a Thermo

Scientific Nicolet iS50 spectrometer (USA) equipped with a custom-designed reaction chamber. For in situ DRIFTS measurements, CW15 was exposed to a mixed flow of O_2, H_2O, and EtOH vapor for 60 min to reach adsorption–desorption equilibrium, followed by 60 min of light irradiation.

2. Photoelectrochemical measurements

Photoelectrochemical measurements were conducted using a CHI 760E electrochemical workstation in a standard three-electrode configuration. An Ag/AgCl electrode served as the reference electrode, whilst a platinum electrode functioned as the counter electrode. Working electrodes were fabricated by uniformly coating fluorine-doped tin oxide (FTO) glass substrates (1.0 cm^2) with a suspension of photocatalyst in ethanol containing 5% Nafion as a binding agent. All electrochemical measurements were performed in 0.5 M Na_2SO_4 electrolyte solution under simulated solar irradiation provided by a 300 W xenon lamp during photocurrent response (I-t) tests.

3. Photocatalytic H_2O_2 production

Photocatalytic performance was assessed by quantifying H_2O_2 formation under simulated solar irradiation. In a typical experiment, 10 mg of catalyst was dispersed in 50 mL of solution (45 mL ultrapure water and 5 mL ethanol) or ultrapure water. The suspension was ultrasonicated for 5 min to ensure uniform dispersion, then purged with O_2 for 30 min to saturate the solution. After establishing adsorption–desorption equilibrium, the reaction was initiated under a 300 W xenon lamp. The distance between the light source and the flask was 20 cm and the light intensity was measured at 0.281 W cm^{-2}. At 15 min intervals, 1 mL aliquots were withdrawn through a 0.22 μm Millipore filter and mixed with 1 mL of 0.4 M KI and 1 mL of 0.1 M potassium hydrogen phthalate ($C_8H_5KO_4$). The mixture was kept in the dark for 30 min to complete the reaction. Absorbance was measured at 350 nm using a Shimadzu UV-1240 spectrophotometer. H_2O_2 concentrations were determined from a pre-established calibration curve (Fig. S4):

$A = 0.00643 \times c + 0.03569$ (1)

where c is the H_2O_2 concentration (μmol L^{-1}) and A is the absorbance at 350 nm. The calibration showed excellent linearity ($R^2 = 0.9999$) using H_2O_2 standards.

1 mmol triethanolamine (TEOA), p-benzoquinone (p-BQ) and isopropanol (IPA) were added into the solution as the trapping agents for h^+, $\cdot O_2^-$ and $\cdot OH$, respectively. Recyclability tests were performed under identical photocatalytic conditions, with the catalyst recovered by centrifugation and washed with deionized water between cycles. H_2O_2 decomposition was examined by dispersing the catalyst in 50 mL of 1 mmol L^{-1} H_2O_2, purging with N_2 to establish an inert atmosphere, and following the same analytical protocol.

4. Computational details

Density functional theory (DFT) calculations were performed using the Vienna Ab initio Simulation Package (VASP). Exchange-correlation effects were treated with the Perdew-Burke-Ernzerhof (PBE) functional within the generalized gradient approximation (GGA) framework. Electron wavefunctions were expanded in a plane-wave basis set with a kinetic energy cutoff of 450 eV. Structural optimizations proceeded until the total energy difference between successive iterations was less than 1.0×10^{-5} eV per atom and the maximum force on any atom fell below 0.03 eV $Å^{-1}$, ensuring robust convergence of the electronic and structural properties.

5. Femtosecond transient absorption spectroscopy (fs-TAS) test

Ultrafast charge carrier dynamics were probed using femtosecond transient absorption spectroscopy (fs-TAS) on a Helios Fire system (Ultrafast Systems LLC) with a maximum time resolution of approximately 8 ns. Catalyst suspensions were prepared by dispersing 5 mg of material in 20 mL of acetonitrile followed by sonication for 20 minutes to ensure homogeneous distribution. Measurements were conducted in a custom-designed quartz cuvette containing 3 mL of the prepared suspension.

The excitation source comprised a regeneratively amplified Ti:sapphire laser system (Coherent Legend) generating 35 fs pulses at 800 nm with 7 mJ pulse^{-1} energy at a 1 kHz repetition rate. The output beam was split into two components: a pump beam frequency-converted to 325 nm via an optical parametric amplifier (OPerA Solo), with power attenuated to 73 μW using neutral density filters; and a probe beam converted to a white-light continuum through a CaF_2 crystal. This configuration enabled precise monitoring of excited-state evolution following photoexcitation, providing detailed insights into the transient electronic structure and charge carrier behavior of the photocatalyst.

6. Average decay time (τ_{ave})

TRPL decay profiles were fitted to a biexponential function:

$$I_{(t)} = I_{(0)} + A_1\exp(-t/\tau_1) + A_2\exp(-t/\tau_2) \quad (2)$$

Where $I_{(0)}$ is the baseline offset, A_1 and A_2 are the pre-exponential amplitudes of the two decay channels, and τ_1 and τ_2 denote the associated lifetimes-assigned to the fast (non-radiative) and slow (radiative) deactivation processes, respectively. The mean lifetime (τ_{ave}) was then calculated by weighting each component according to its contribution:

$$\tau_{ave} = (A_1\tau_1^2 + A_2\tau_2^2)/(A_1\tau_1 + A_2\tau_2) \quad (3)$$

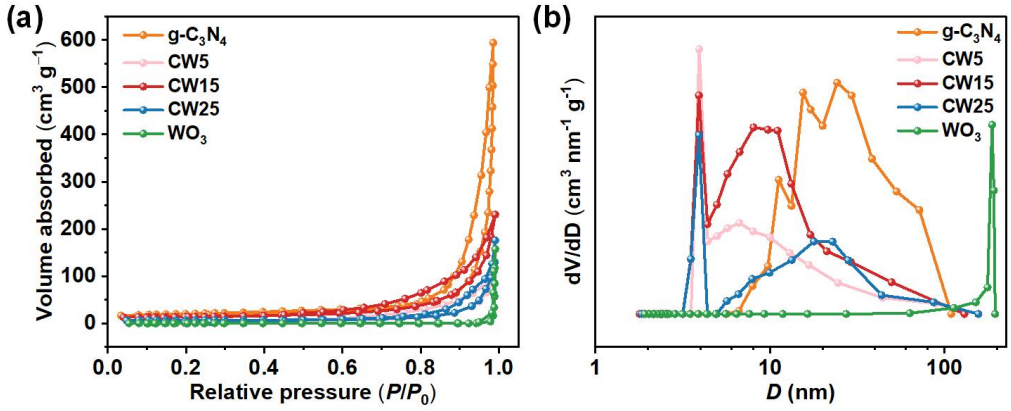

Fig.S1. (a) N_2 adsorption–desorption isotherms and (b) corresponding pore-size distributions of g-C_3N_4, WO_3, and g-C_3N_4/WO_3 composites.

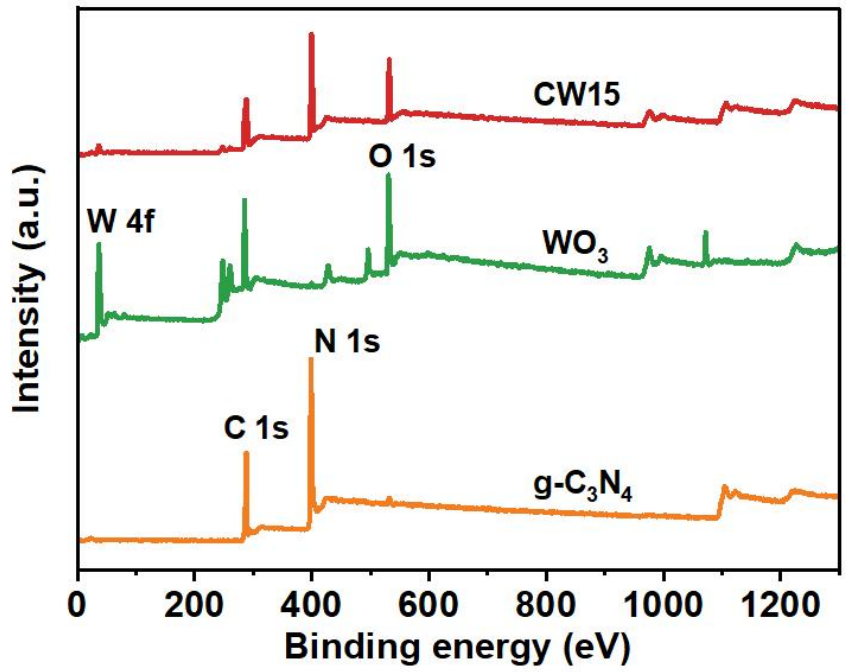

Fig.S2. XPS survey spectra of g-C_3N_4, WO_3, and CW15.

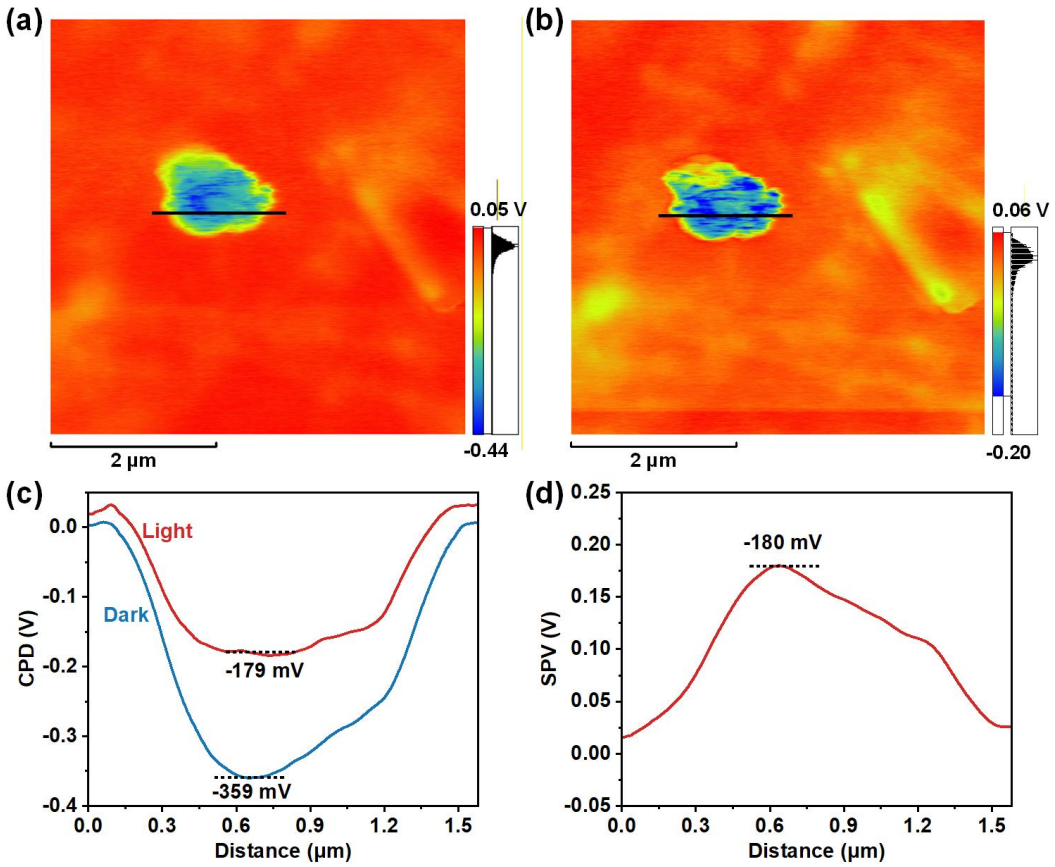

Fig. S3. KPFM images of g-C_3N_4 (a) in the dark and (b) under light illumination. The corresponding (c) V_{CPD} and (d) SPV of g-C_3N_4 along the marked line.

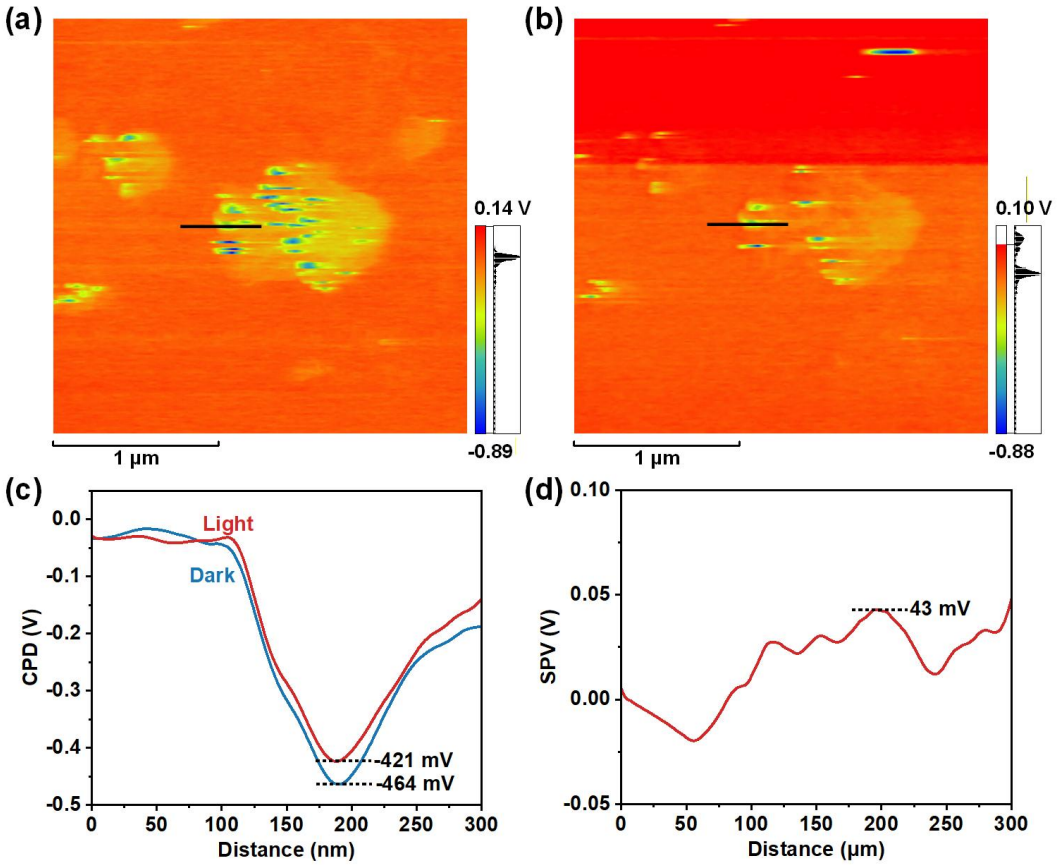

Fig. S4. KPFM images of WO_3 (a) in the dark and (b) under light illumination. The corresponding (c) V_{CPD} and (d) SPV of WO_3 along the marked line.

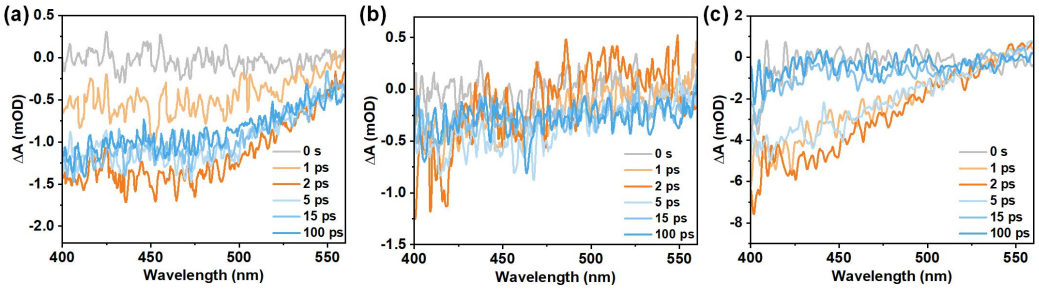

Fig. S5. TA spectra of (a) g-C_3N_4, (b) WO_3, and (c) the CW15 composite at selected time delays following excitation with a 325 nm pump pulse.

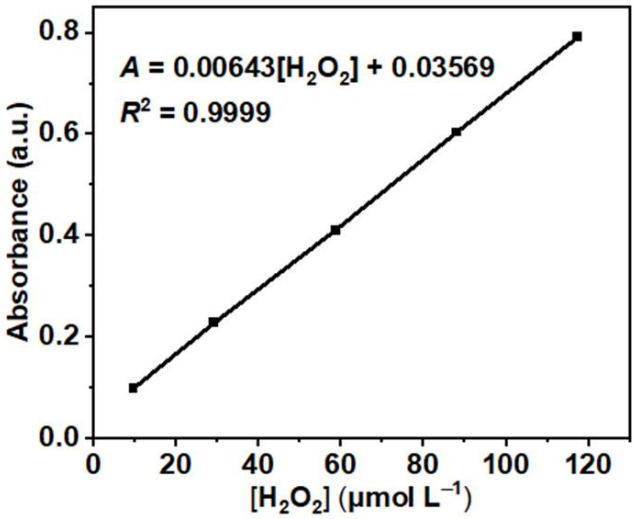

Fig.S6. Relationship between the concentration of H_2O_2 and its absorbance intensity.

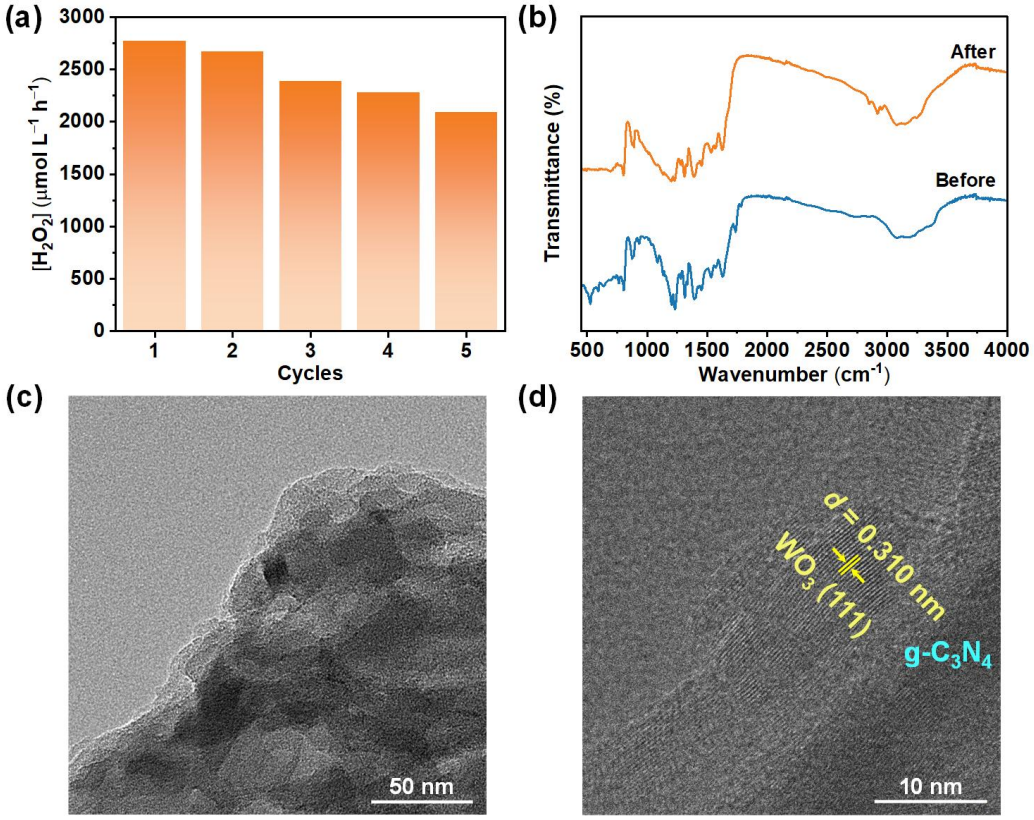

Fig. S7. (a) Cycling performance and (b) FTIR spectra of the catalyst before and after the reaction. (c) TEM and (d) HRTEM images of CW15 after five consecutive photocatalytic cycles.

Table S1. BET surface area (S_{BET}), pore volume (PV), and average pore size (APS) derived from Fig. S1.

Samples	S_{BET} ($m^2\ g^{-1}$)	PV ($cm^3\ g^{-1}$)	APS (nm)
g-C_3N_4	67	0.92	54.9
CW5	17	0.18	43.2
CW15	46	0.35	30.7
CW25	20	0.22	44.2
WO_3	1	0.19	1095.3

Table S2. Fitting parameters and average lifetimes (τ_a) of TRPL.

Samples	τ_1 (ns)	A_1 (%)	τ_2 (ns)	A_2 (%)	τ_a (ns)
g-C_3N_4	0.11	57.1	3.04	42.9	2.90
CW15	0.18	95.4	3.16	4.6	1.55
WO_3	0.15	80.3	3.51	19.7	3.02

Table S3. The V_{CPD} and SPV of g-C_3N_4, WO_3, g-C_3N_4-CW15, and WO_3-CW15.

Samples	$V_{CPD\text{-}Dark}$ (mV)	$V_{CPD\text{-}Light}$ (mV)	SPV (mV)
g-C_3N_4	–359	–179	180
WO_3	–464	–421	43
g-C_3N_4-CW15	–265	–141	124
WO_3-CW15	–300	–193	107

Table S4. Decay lifetimes extracted by fitting the decay kinetics at 430 nm for g-C_3N_4 and CW15 in Fig. 9d, and at 420 nm for pristine WO_3 in Fig. 9e.

Samples	τ_1 (ps)	A_1 (%)	τ_2 (ps)	A_2 (%)	τ_3 (ps)	A_3 (%)	τ_a (ps)
g-C_3N_4	255.0	57.0	1094.3	43.0			896.5
CW15	196.4	21.3	46.1	28.9	4.5	49.8	154.0
WO_3	278.8	30.5	1563.1	69.5			1470.0

Table S5. Comparison of H_2O_2 production rate of TT30 with other catalysts.

Catalyst	Lamp source	Scavenger	H_2O_2 production ($\mu mol\ g^{-1}\ h^{-1}$)	References
Gd-WO_3	Xenon lamp	tetracycline	580	[1]
$Au_{0.5}/WO_3$	Metal halide lamp	Methanol	108.8	[2]
WO_3/SnO_2	Metal halide lamp	Ethanol	57.4	[3]
S-doped g-C_3N_4/TiO_2	Xenon lamp	H_2O	2128	[4]
Ba_2AgIO_6/C_3N_4	Xenon lamp	H_2O	535.9	[5]
g-C_3N_4/BiOBr	Xenon lamp	Ethanol	1176	[6]
TiO_{2-x}/g-C_3N_{4-x}	Xenon lamp	Ethanol	2829	[7]
TiO_2/COF	Xenon lamp	RhB	1326	[8]
Cu-N doped -GO/C_3N_4	Xenon lamp	Ethanol	2856	[9]
g-C_3N_4/WO_3	Xenon lamp	Ethanol	2571.6	This work

References

[1] J. Wang, J. Wang, S. Zuo, J. Pei, W. Liu, J. Wang, *Chin. Chem. Lett.*, **2023**, 34, 108157.

[2] Y. Wang, Y. Wang, J. Zhao, M. Chen, X. Huang, Y. Xu, *Appl. Catal.*, B, **2021**, 284, 119691.

[3] D. Xie, C. Chen, Y. Wang, C. Sun, Y. Xu, J. Huang, *J. Mater. Chem. A*, **2024**, 12, 11612-11624.

[4] Z. Jiang, Q. Long, B. Cheng, R. He, L. Wang, *J. Mater. Sci. Technol.*, **2023**, 162, 1-10.

[5] K. Yang, Z. Song, X. Fu, W. Yan, T. Zhang, Y. Hua, H. Lin, Q. Kuang, Z. Xie, *Inorg. Chem. Front.*, **2025**, DOI: 10.1039/D5QI01052G.

[6] T. Cao, Q. Xu, J. Zhang, S. Wang, T. Di, Q. Deng, *Chin. J. Catal.*, **2025**, 72, 118-129.

[7] J. Gao, S. Yang, P. Wei, S. Wang, L. Zheng, L. Lan, y. Wang, Y. Li, C. Chen, G. He, Y. Liu, *Sep. Purif. Technol.*, **2025**, 354, 128685.

[8] Y. Zhao, Y. Zhang, H. Tan, C. Ai, J. Zhang, *J. Materiomics*, **2025**, 11, 100970.

[9] H. Li, B. Zhu, B. Cheng, G. Luo, J. Xu, S. Cao, *J. Mater. Sci. Technol.*, **2023**, 161, 192-200.